analytical chemistry

pubs.acs.org/ac Article

# Bandgap-Regulated Electrochemiluminescence Enhancement Strategy for Florfenicol Detection Based on $ZrCuO_3$: A Multimodal Luminophore

Xue Dong, Xiaoyue Zhang, Xiang Ren, Hongmin Ma, Nuo Zhang,* Faying Li,* Huangxian Ju, and Qin Wei*

Cite This: *Anal. Chem.* 2023, 95, 17362−17371 Read Online

ACCESS | Metrics & More | Article Recommendations | Supporting Information

**ABSTRACT:** The low electrochemiluminescence (ECL) efficiency issue of zirconia ($ZrO_2$) has been a pressing problem since its discovery. In this study, a bandgap-regulated ECL enhancement strategy was developed to improve the ECL efficiency of $ZrO_2$. Specifically, through the calcination of metal−organic frameworks (MOFs), the MOF-derived bimetallic oxide $ZrCuO_3$ was synthesized. Compared to $ZrO_2$, the synthesized $ZrCuO_3$ exhibited a narrower bandgap and higher electron transfer efficiency, leading to enhanced ECL efficiency. Further investigation of the ECL emitter revealed that $ZrCuO_3$ exhibited multimodal ECL emission: annihilation ECL and co-reactant participation ECL (including anodic ECL with tripropylamine as a co-reactant and cathodic ECL with $K_2S_2O_8$ as a co-reactant). The anodic ECL with the highest efficiency was selected as the main mode for detecting the target in the aptasensor. Annihilation ECL and cathodic ECL served as alternative modes to ensure stability and continuity of the sensing system. Based on the bandgap-regulated strategy of $ZrCuO_3$, a sensing chip with ITO as the working electrode was designed for the sensitive detection of florfenicol (FF). The constructed signal "off−on−off" aptasensor exhibited excellent detection performance for FF in the range of 0.0005−200 ng/mL. The proposed method provided a novel strategy for the analysis of other antibiotics or biomolecules.

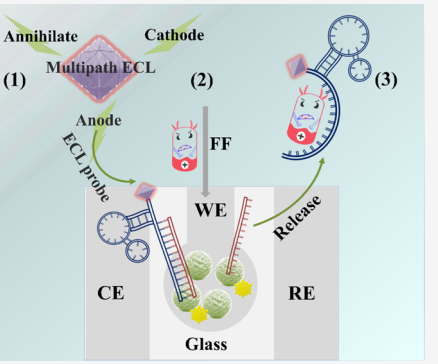


## INTRODUCTION

Florfenicol (FF) is an injectable antibiotic that belongs to the fluoroquinolone class of drugs. It is extensively used in aquaculture to treat various fish diseases.[1,2] In recent years, there has been a growing concern about the potential environmental impacts of fluoroquinolones, particularly on aquatic organisms.[3−5] FF can bioaccumulate in fish and other aquatic species, which poses a risk to human health when consuming seafood.[6−8] There have been calls for increased regulation of fluoroquinolone use in agriculture and food production. Consequently, it is crucial to detect FF residues in fish, other food sources, and the water environment to safeguard human health. FF has been analyzed and detected by using a variety of methods including fluorescence, colorimetry, electrochemiluminescence (ECL), and other methods. ECL technology has received widespread attention due to its strong anti-interference ability and high sensitivity.[9−12]

Zr-based oxides, primarily zirconia ($ZrO_2$), have found extensive applications in various domains owing to their excellent biocompatibility, catalytic activity, and photochemical reactivity.[13−18] The cathode and anode ECL properties of $ZrO_2$ have been successively reported.[19,20] However, the report has shown that the ECL efficiency of $ZrO_2$ is not satisfactory. One of the possible reasons is that the bandgap energy of $ZrO_2$ is large, which limits the ability of electrons to move within its lattice, thereby affecting the excitation and emission efficiency of electrons. Bandgap-regulated enhancement strategies can effectively address the issue of low ECL efficiency in $ZrO_2$ caused by its wide bandgap. In this study, bimetallic oxides were obtained by calcining bimetallic metal−organic frameworks (MOFs), which enabled effective reduction of the bandgap of the emitter. The bandgap-regulated strategy led to improved electron transfer efficiency and enhanced ECL performance in the luminophore.

In numerous reports, an ECL reagent typically exhibits only single-type or single-modal ECL emission, which can be categorized as annihilation ECL and co-reactant participation ECL.[21−27] Co-reactant participation ECL includes anodic emission with tripropylamine (TPrA) as the co-reactant and cathodic emission with $K_2S_2O_8$ as the co-reactant, among others. However, single-modal ECL emission may lead to

Received: August 25, 2023
Revised: October 25, 2023
Accepted: October 29, 2023
Published: November 16, 2023







https://doi.org/10.1021/acs.analchem.3c03823
*Anal. Chem.* 2023, 95, 17362−17371

Scheme 1. (A) Fabrication Scheme of ECL Aptasensor and (B) the Synthesis of $ZrCuO_3$

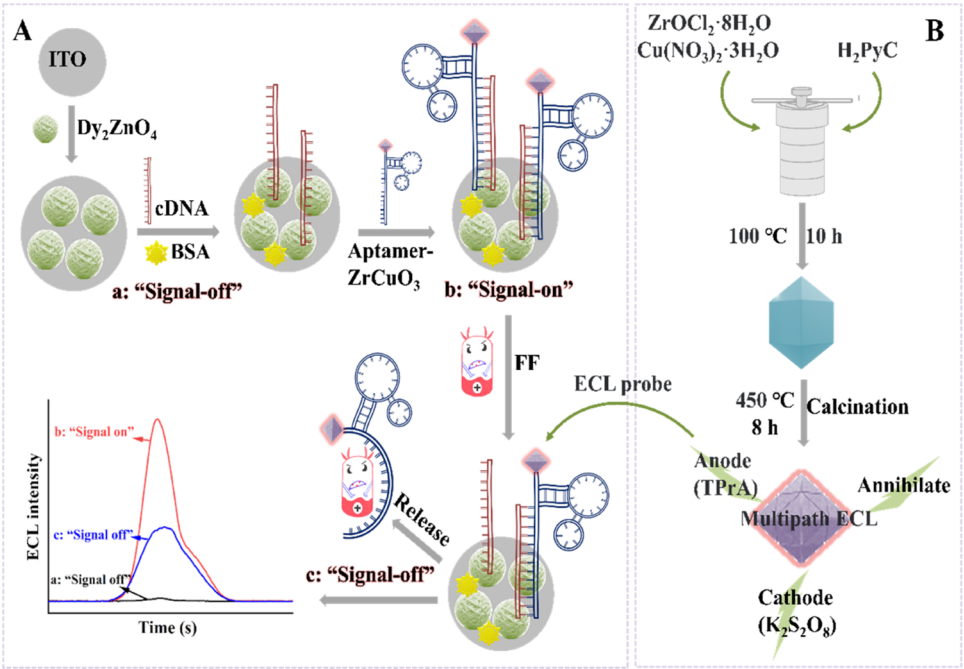


inaccurate output information due to environmental factors, operational errors, and other variables. Multimodal ECL emission refers to a phenomenon where the luminophore exhibits multiple properties of annihilation ECL and co-reactant participation ECL.[28−31] Luminophores with multimodal ECL emission offer several advantages: (1) The most suitable analysis mode is allowed to be selected for different targets during analysis and detection, thereby significantly improving the applicability and operability of the luminophore in various environments; (2) Multimodal ECL emitter can be used to construct multisignal sensors, where multiple ECL responses can mutually validate each other, thereby improving the accuracy and reliability of the sensor; (3) In the case of using only one mode as the signal output source, an alternative ECL mode can be utilized as a substitute. If an error occurs within the main mode, then the secondary mode can be promptly switched to ensure the stability and continuity of the detection system.

In this study, $ZrCuO_3$ nanomaterials were synthesized by calcining bimetallic MOFs. Compared to the wide bandgap of $ZrO_2$ (4.19 eV), $ZrCuO_3$ exhibited a narrower bandgap of 2.55 eV. The narrower bandgap implied a higher electron transfer efficiency and facilitated electron excitation, thereby endowing $ZrCuO_3$ with an intrinsic self-enhancement capability in ECL efficiency. Under different experimental conditions, $ZrCuO_3$ showcased multimodal ECL emission. $ZrCuO_3$ was employed as the ECL probe, with the anodic emission exhibiting the highest ECL efficiency, selected as the primary detection mode for the aptasensor. Additionally, $Dy_2ZnO_4$ as a co-reactant accelerator was introduced into the sensing system to further enhance the ECL performance and sensitivity of the aptasensor.[32−35] Based on the aforementioned strategy, a sensitive aptasensor chip with the signal "off−on−off" was developed to detect FF.

## EXPERIMENTAL SECTION

Detailed descriptions of the reagents and materials, apparatus, the measurement parameters of ECL aptasensor, and electrochemical measurement parameters are displayed in the Supporting Information.

**Synthesis of $ZrCuO_3$ and Aptamer-$ZrCuO_3$.** The bimetallic ZrCu-MOF was synthesized according to the literature.[36] First, 42.5 mg of $ZrOCl_2·8H_2O$, 124 mg of $Cu(NO_3)_2·3H_2O$, and 32.5 mg of $H_2PyC$ were dissolved in 10 mL of DMF and mixed uniformly. Then, 120 $\mu$L of TFA was added to the mixture. The mixture was kept at 100 °C for 10 h and the obtained ZrCu-MOF was centrifuged and washed with DMF and ethanol. The dried ZrCu-MOF was placed in a muffle furnace and kept at 450 °C for 8 h with a heating/cooling rate of 2 °C/min. The resulting product obtained from the described process was $ZrCuO_3$. 4 mg of $ZrCuO_3$ was mixed with 1 mL of aptamer solution (10 $\mu$mol/L) and oscillated for 12 h. After centrifugation and washing, the aptamer-$ZrCuO_3$ complex was obtained.

**Synthesis of $Dy_2ZnO_4$.** DyZn-MOF was first synthesized according to the literature with specific steps as follows:[37] A solvent with a pH of 5.7 was prepared by combining sodium acetate and acetic acid in a suitable proportion. Then, 0.05 mmol of $DyCl_3·6H_2O$, 0.1 mmol of zinc acetate, and 0.5 mmol of $H_3$imdc were dissolved in the prepared solvent (4 mL). Subsequently, 2 mL of deionized water was added to the mixture, which was then maintained at 180 °C for 24 h. Afterward, DyZn-MOF was obtained through multiple centrifugations and washing steps using deionized water and ethanol. Finally, DyZn-MOF was placed in a muffle furnace and maintained at 550 °C for 4 h (at a heating/cooling rate of 2 °C/min), resulting in the formation of $Dy_2ZnO_4$.

**Construction of Aptasensor.** The sensing chip was fabricated on a 3 cm × 3 cm glass substrate. Indium tin oxide (ITO) was sputtered onto the glass substrate by using magnetron sputtering, which served as the working electrode (WE). Both the counter electrode (CE) and the reference


https://doi.org/10.1021/acs.analchem.3c03823
Anal. Chem. 2023, 95, 17362−17371

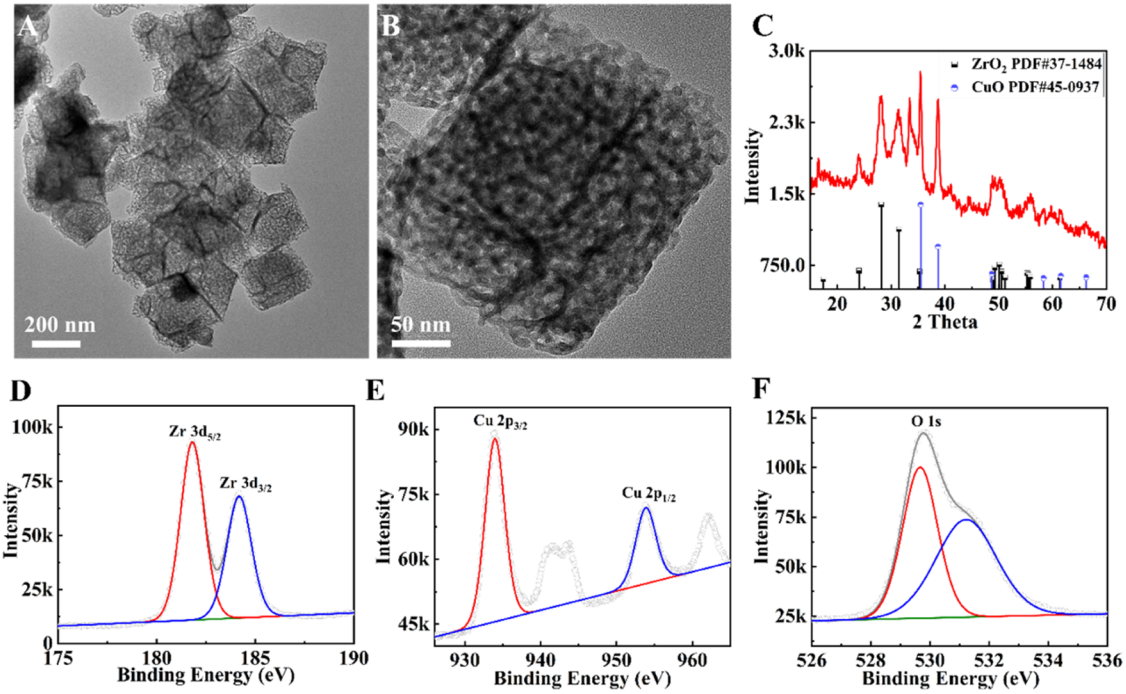


**Figure 1.** (A) TEM image, (B) HRTEM image, (C) XRD spectrum of $ZrCuO_3$; and XPS spectra of $ZrCuO_3$: (D) Zr 3d, (E) Cu 2p and (F) O 1s.

electrode (RE) were prepared by screen printing conductive carbon paste and Ag/AgCl paste onto the glass substrate. The specific fabrication process of the aptasensor is shown in Scheme 1. First, 15 $\mu$L of $Dy_2ZnO_4$ was dropped onto the sensing chip, followed by the addition of 15 $\mu$L of cDNA, 5 $\mu$L of BSA, and 15 $\mu$L of aptamer-$ZrCuO_3$. Finally, the modified electrode was immersed in different concentrations of FF solution to construct a signal "off−on−off" aptasensor. It should be noted that unbound biomolecules should be rinsed off with PBS (pH 7.4).

## RESULTS AND DISCUSSION

**Characterization of $ZrCuO_3$ and $Dy_2ZnO_4$.** $ZrCuO_3$ and $Dy_2ZnO_4$ were characterized for their crystal structures, morphologies, and chemical compositions using multiple techniques. As shown in Figure S1, the synthesized Zr−Cu bimetallic MOF exhibited a polyhedral shape with a diameter of approximately 550 nm. After calcination, $ZrCuO_3$ maintained a cubic morphology but significantly decreased in size compared to the MOF, measuring around 300 nm (Figure 1A). Moreover, from the high-resolution TEM image (HRTEM) of a single cube, it could be observed that the initially dense and intact MOF structure transformed into a loose particle state (Figure 1B) after calcination, which may be attributed to disruption of the Zr−Cu MOF framework at high temperatures. The elemental distribution of $ZrCuO_3$ was tested, and the results showed that the Zr, Cu, and O elements were evenly distributed in Figure S2. Additionally, XRD analysis was performed to determine the crystal structure of $ZrCuO_3$, and the diffraction peaks of $ZrCuO_3$ corresponded precisely to those of $ZrO_2$ (PDF#37−1484) and CuO (PDF#45−0937) standard cards (Figure 1C). Furthermore, $ZrCuO_3$ exhibited a relatively large specific surface area of 75.79 $m^2/g$ and a pore size of approximately 18.3 nm (Figure S3). X-ray photoelectron spectroscopy (XPS) analysis was conducted to investigate the surface elemental composition of $ZrCuO_3$. The peaks at binding energies of 181.81 and 184.19 eV corresponded to Zr $3d_{5/2}$ and Zr $3d_{3/2}$ of $Zr^{4+}$, respectively (Figure 1D), whereas the peaks at 933.96 and 953.87 eV represented Cu $2p_{3/2}$ and Cu $2p_{1/2}$ of $Cu^{2+}$, respectively (Figure 1E). The peaks located at 529.67 and 531.22 eV in the O 1s spectrum were attributed to lattice oxygen and surface oxygen in the metal oxide, respectively (Figure 1F).

DyZn-MOF, as observed in Figure 2A−2C, was composed of numerous nanofibers assembled into spherical structures with a diameter of approximately 3−5 $\mu$m. After calcination, $Dy_2ZnO_4$ clearly showed that the nanofibers had been destroyed and transformed into a denser structure with a diameter of 2−4 $\mu$m (Figure 2D−2F). The XRD spectrum in Figure 3A confirmed that $Dy_2ZnO_4$ corresponded completely to the XRD standard cards of $Dy_2O_3$ (PDF#43−1006) and ZnO (PDF#36−1451). HRTEM also revealed the (222) crystal plane of $Dy_2O_3$ (Figure 2G). Selected area diffraction of $Dy_2ZnO_4$ further verified the (222) crystal plane of $Dy_2O_3$ and the (100), (101), (102), and (110) crystal planes of ZnO (Figure 2H, a−e). The elemental mapping image of $Dy_2ZnO_4$ exhibited a homogeneous distribution of Dy, Zn, and O (Figure 2I). XPS spectra were employed for elemental valence state analysis of $Dy_2ZnO_4$. The full spectrum of $Dy_2ZnO_4$ demonstrated that the composite consisted of Dy, Zn, and O as the major elements (Figure 3B). Two peaks located at 1021.58 and 1044.65 eV represented Zn $2p_{3/2}$ and Zn $2p_{1/2}$ of $Zn^{2+}$, respectively (Figure 3C). The Dy 3d (Figure 3D) and 4d (Figure 3E) orbitals were also examined, with Dy $3d_{5/2}$ and Dy $3d_{3/2}$ orbitals appearing at 1297.70 and 1336.11 eV, respectively. While the double peaks at binding energies of 155.41 and 152.26 eV were attributed to Dy 4d orbitals,[38,39] the peaks at 529.05 and 531.07 eV in the O 1s spectrum were ascribed to lattice oxygen and surface hydroxyl groups of the metal oxide, respectively (Figure 3F).

**Multimodal ECL Emission of $ZrCuO_3$.** An in-depth exploration was conducted on the ECL properties of $ZrCuO_3$ under different experimental parameters and testing solutions.


https://doi.org/10.1021/acs.analchem.3c03823
Anal. Chem. 2023, 95, 17362−17371

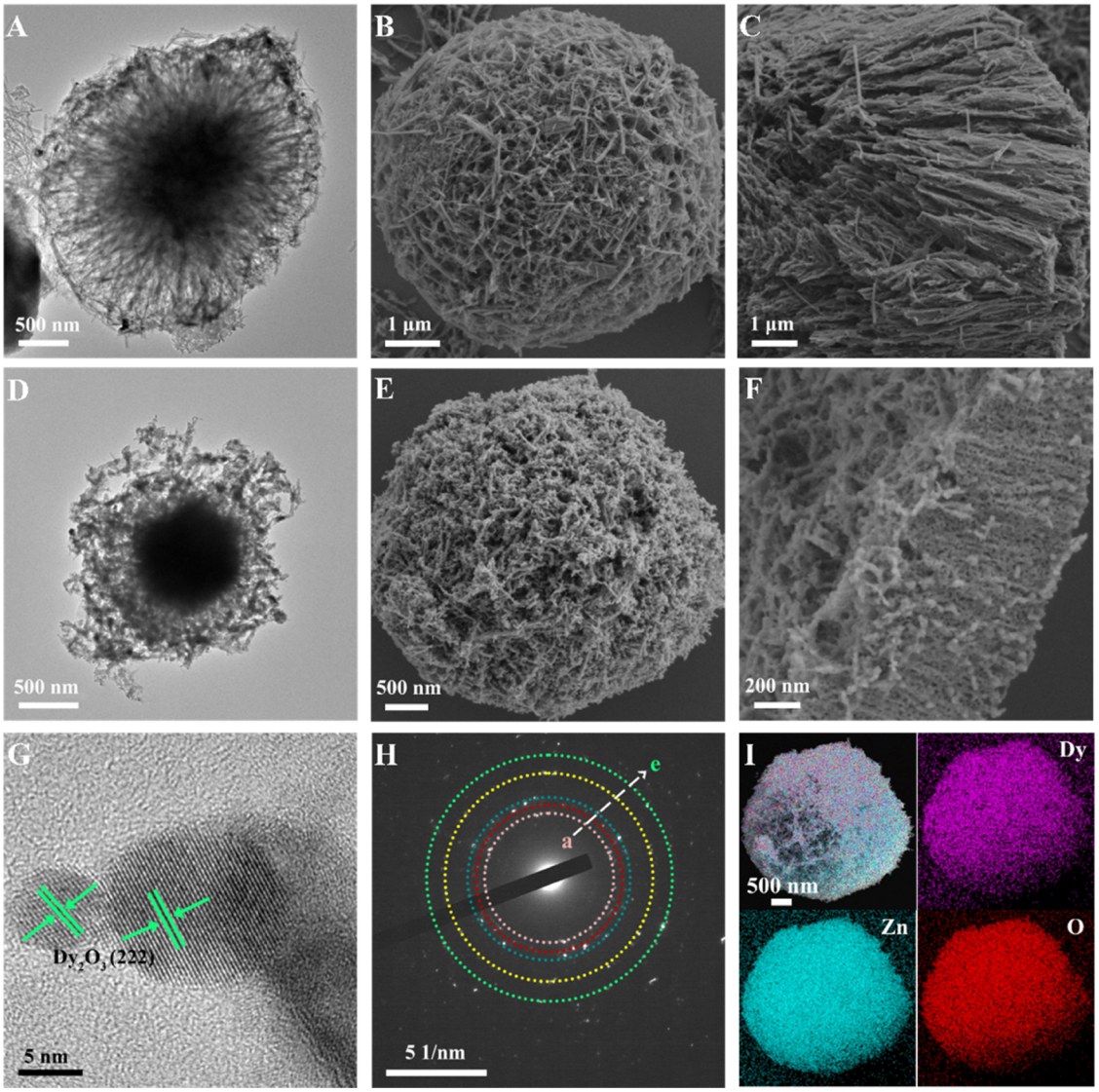


**Figure 2.** (A) TEM image and (B, C) SEM images of DyZn-MOF; (D) TEM image, (E, F) SEM images, (G) HRTEM, (H) selected area diffraction image and (I) mapping images of $Dy_2ZnO_4$.

Multimodal ECL emission in $ZrCuO_3$ was successfully identified, including annihilation ECL, anodic ECL emission with TPrA as the co-reactant, cathodic ECL emission with $K_2S_2O_8$ as the co-reactant.

The annihilation ECL of $ZrCuO_3$ was examined at a scanning voltage range of −2 to 2 V. As shown in Figure 4A,B, $ZrCuO_3$ exhibited regular ECL emissions in the PBS (pH 7.4). Based on the experimental observations and previous literature, a preliminary hypothesis was proposed for the annihilation ECL mechanism of $ZrCuO_3$:[40] during cyclic scanning from positive to negative voltages, electron gain and loss occurred in $ZrCuO_3$, resulting in the generation of $ZrCuO_3^{\bullet+}$ and $ZrCuO_3^{\bullet-}$ species (eqs 1 and 2). The subsequent reaction between these species led to the formation of the excited state $ZrCuO_3$* (eq 3), which then emitted photons and returned to the ground state (eq 4).

$$ZrCuO_3 \rightarrow ZrCuO_3^{\bullet+} + e^- \quad (1)$$

$$ZrCuO_3 + e^- \rightarrow ZrCuO_3^{\bullet-} \quad (2)$$

$$ZrCuO_3^{\bullet+} + ZrCuO_3^{\bullet-} \rightarrow ZrCuO_3^* \quad (3)$$

$$ZrCuO_3^* \rightarrow ZrCuO_3 + h\nu \quad (4)$$

Subsequently, the cathodic ECL properties of $ZrCuO_3$ were investigated. Under the testing conditions of a scanning potential range from 0 to −1.6 V and using 80 mmol/L of $K_2S_2O_8$ as a co-reactant, $ZrCuO_3$ exhibited stable ECL emission with the intensity of approximately 1800 au (Figure 4C). Figure 4D displays the reduction peaks of the $ZrCuO_3$/$K_2S_2O_8$ system appearing at −1.20 and −1.45 V. Based on these findings, a hypothesis was proposed for the cathodic ECL mechanism of the $ZrCuO_3/K_2S_2O_8$ system:[19,41] $S_2O_8^{2-}$ and $ZrCuO_3$ gained electrons to form $SO_4^{\bullet-}$ and $ZrCuO_3^{\bullet-}$ (eqs 5 and 6), respectively. The interaction between $SO_4^{\bullet-}$ and $ZrCuO_3^{\bullet-}$ resulted in the formation of the excited state $ZrCuO_3$* (eq 7), which released energy in the form of the luminous signal before returning to the ground state (eq 8).

$$S_2O_8^{2-} + e^- \rightarrow SO_4^{2-} + SO_4^{\bullet-} \quad (5)$$

$$ZrCuO_3 + e^- \rightarrow ZrCuO_3^{\bullet-} \quad (6)$$



https://doi.org/10.1021/acs.analchem.3c03823
Anal. Chem. 2023, 95, 17362−17371

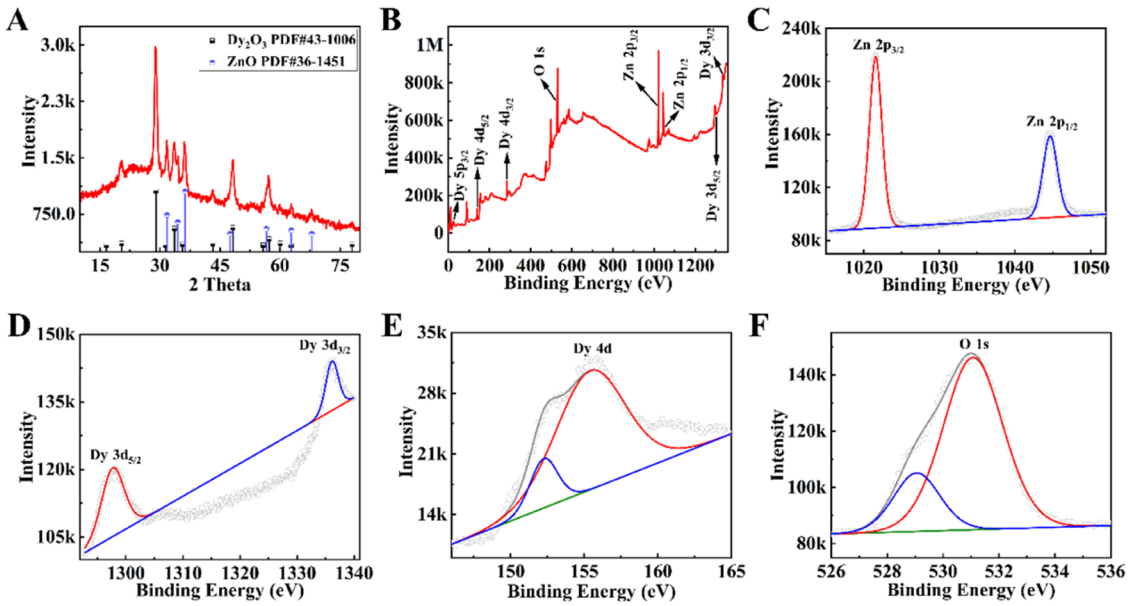


**Figure 3.** (A) XRD spectrum of $Dy_2ZnO_4$; XPS spectra of $Dy_2ZnO_4$: (B) full spectrum, (C) Zn 2p, (D) Dy 3d, (E) Dy 4d, and (F) O 1s.

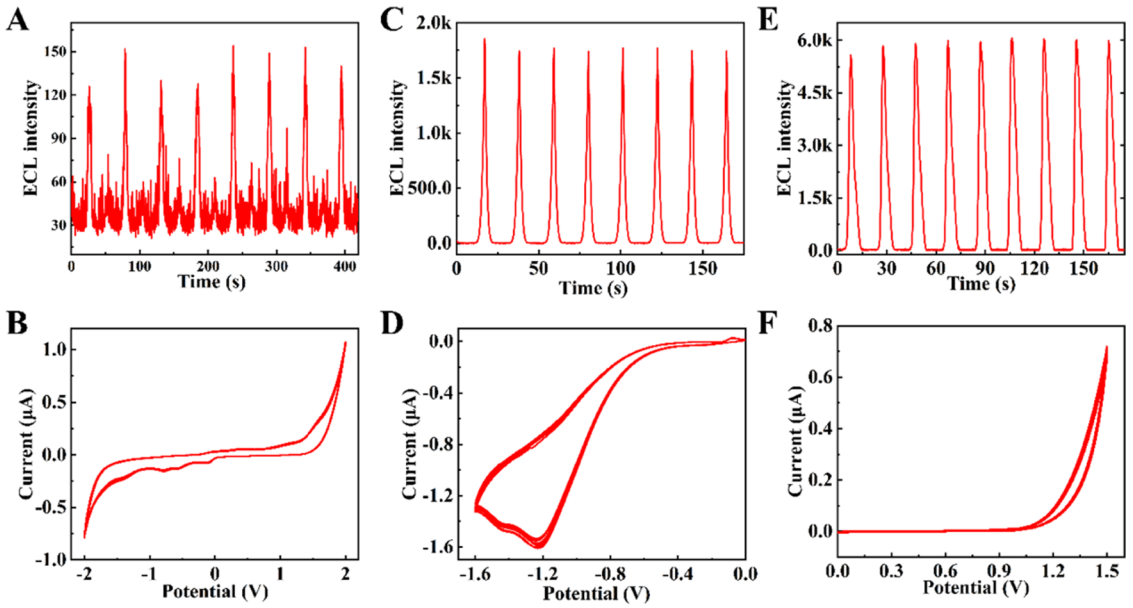


**Figure 4.** (A) Annihilation ECL and (B) corresponding CV, (C) cathodic ECL and (D) corresponding CV, and (E) anodic ECL and (F) corresponding CV of $ZrCuO_3$.

$$ZrCuO_3^{\bullet -} + SO_4^{\bullet -} \rightarrow ZrCuO_3^{*} + SO_4^{2-} \quad (7)$$

$$ZrCuO_3^{*} \rightarrow ZrCuO_3 + h\nu \quad (8)$$

The third emission mode of $ZrCuO_3$, the anodic ECL, was thoroughly investigated. Under cyclic voltammetry scanning from 0 to 1.5 V, the anodic ECL emission of $ZrCuO_3$ was tested using TPrA as the co-reactant. As shown in Figure 4F, the current value started to increase around 1 V. The anodic ECL signal of $ZrCuO_3$ was approximately 6000 au (Figure 4E). Based on previous literature, the proposed mechanism for the anodic ECL of $ZrCuO_3$ was as follows:[20] TPrA and $ZrCuO_3$ were oxidized separately (eqs 9 and 10), and the oxidation product $TPrA^{\bullet +}$ underwent deprotonation to generate the intermediate $TPrA^{\bullet}$ (eq 11). $TPrA^{\bullet}$ further reacted with $ZrCuO_3^{\bullet +}$ to reach $ZrCuO_3$* (eq 12), which subsequently released energy to generate the ECL signal (eq 13).

$$TPrA \rightarrow TPrA^{\bullet +} + e^{-} \quad (9)$$

$$ZrCuO_3 \rightarrow ZrCuO_3^{\bullet +} + e^{-} \quad (10)$$

$$TPrA^{\bullet +} \rightarrow TPrA^{\bullet} + H^{+} \quad (11)$$

$$ZrCuO_3^{\bullet +} + TPrA^{\bullet} \rightarrow ZrCuO_3^{*} \quad (12)$$

$$ZrCuO_3^{*} \rightarrow ZrCuO_3 + h\nu \quad (13)$$

**Investigation on the Enhanced ECL of $ZrCuO_3$.** ECL emissions from different modified electrodes were tested using TPrA as a co-reactant. As shown in Figure 5A, the bare electrode (curve a) and CuO derived from Cu MOF


https://doi.org/10.1021/acs.analchem.3c03823
Anal. Chem. 2023, 95, 17362−17371

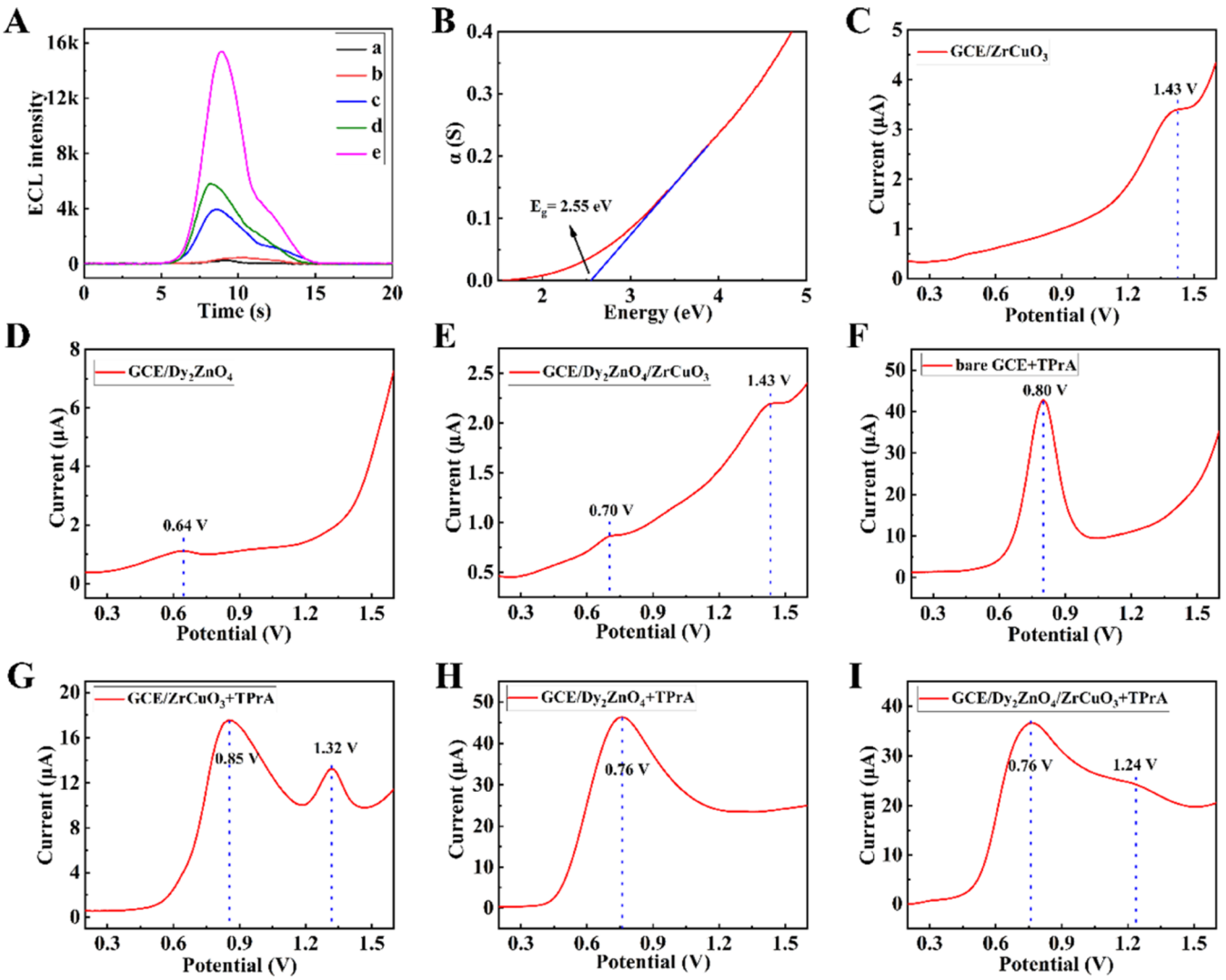


**Figure 5.** (A) ECL intensity of bare electrode (curve a), CuO (curve b), $ZrO_2$ (curve c), $ZrCuO_3$ (curve d), and $Dy_2ZnO_4/ZrCuO_3$ (curve e); (B) bandgap of $ZrCuO_3$; DPV of (C) $ZrCuO_3$, (D) $Dy_2ZnO_4$, and (E) $Dy_2ZnO_4/ZrCuO_3$ in PBS (pH 7.4); DPV of (F) bare electrode, (G) $ZrCuO_3$, (H) $Dy_2ZnO_4$, and (I) $Dy_2ZnO_4/ZrCuO_3$ in PBS (pH 7.4) containing TPrA.

calcination (curve b) did not exhibit ECL emission. In contrast, the ECL intensity of $ZrO_2$ and $ZrCuO_3$ reached approximately 4000 au (curve c) and 6000 au (curve d), respectively. Compared to $ZrO_2$, $ZrCuO_3$ showed a significant enhancement in the ECL intensity. Through analysis of the measured ultraviolet−visible (UV−vis) absorption spectroscopy data, the bandgap values of $ZrO_2$ (Figure S4) and $ZrCuO_3$ (Figure 5B) were determined as 4.19 and 2.55 eV, respectively. This indicated that the narrower bandgap could enhance the electron transport rate, thereby promoting the excitation of $ZrCuO_3$ and improving its ECL performance.

Subsequently, ECL tests were performed on the $Dy_2ZnO_4/ZrCuO_3$-modified electrode. Figure 5A illustrates that the ECL signal of the modified electrode was increased to approximately 16 000 au (curve e). The addition of $Dy_2ZnO_4$ greatly enhanced the ECL signal of $ZrCuO_3$. Differential pulse voltammetry (DPV) measurements were conducted on different modified electrodes in various testing solutions to further investigate the anodic ECL of $ZrCuO_3$ and the enhancing mechanism of $Dy_2ZnO_4$.[42] In PBS, the bare electrode did not exhibit any oxidation peak (Figure S5). Conversely, the $ZrCuO_3^-$ modified electrode demonstrated an oxidation peak at 1.43 V in PBS, confirming the process of electron loss and oxidation in $ZrCuO_3$ (eq 9) (Figure 5C). Similarly, the $Dy_2ZnO_4$-modified electrode displayed an oxidation peak at 0.64 V in PBS, indicating that $Dy_2ZnO_4$ could lose electrons and undergo oxidation (Figure 5D). The $Dy_2ZnO_4/ZrCuO_3$-modified electrode displayed oxidation reactions of both species (Figure 5E). Upon the addition of the co-reactant TPrA, the bare electrode exhibited an oxidation peak at 0.8 V (eq 10) (Figure 5F). Furthermore, the oxidation peak of $ZrCuO_3$ in TPrA-containing PBS was observed at 1.32 V (Figure 5G). In comparison to the bare electrode, the $Dy_2ZnO_4$-modified electrode demonstrated a broader oxidation peak at 0.76 V in the TPrA solution (Figure 5H), indicating that the presence of $Dy_2ZnO_4$ promoted the oxidation of TPrA. The $Dy_2ZnO_4/ZrCuO_3$-modified electrode exhibited two oxidation peaks at 0.76 and 1.24 V, further confirming the promotion of TPrA and $ZrCuO_3$ oxidation by $Dy_2ZnO_4$ (Figure 5I). Based on the experimental results, the following possible mechanisms for the ECL enhancement of $Dy_2ZnO_4$ were proposed: $Dy_2ZnO_4$ acted as a co-reactant accelerator, effectively enhancing the oxidation of TPrA and increasing the production of $TPrA^{\bullet+}$, thus enhancing the ECL


https://doi.org/10.1021/acs.analchem.3c03823
Anal. Chem. 2023, 95, 17362−17371

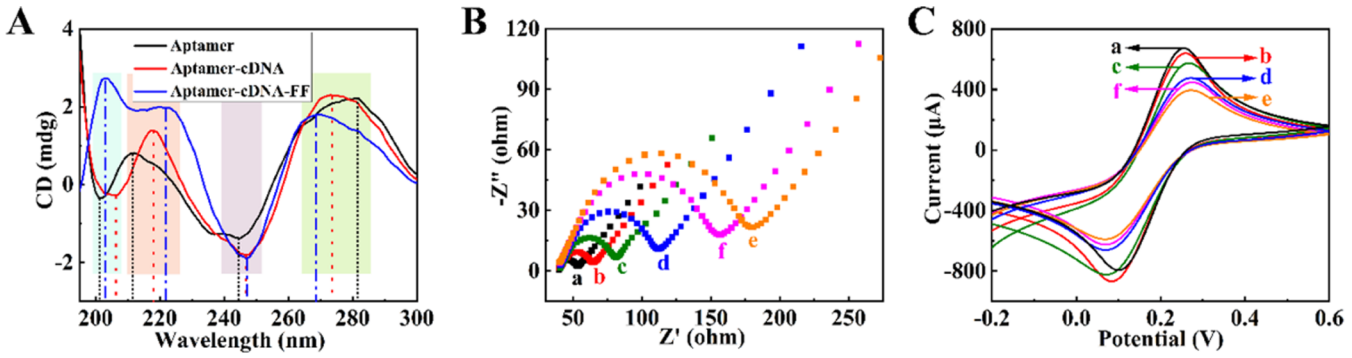


**Figure 6.** (A) CD spectrum; (B) EIS and (C) CV of bare electrode (a), $Dy_2ZnO_4$ (b), $Dy_2ZnO_4$/cDNA (c), $Dy_2ZnO_4$/cDNA/BSA (d), $Dy_2ZnO_4$/cDNA/BSA/aptamer-$ZrCuO_3$ (e), and $Dy_2ZnO_4$/cDNA/BSA/aptamer-$ZrCuO_3$/FF (f).

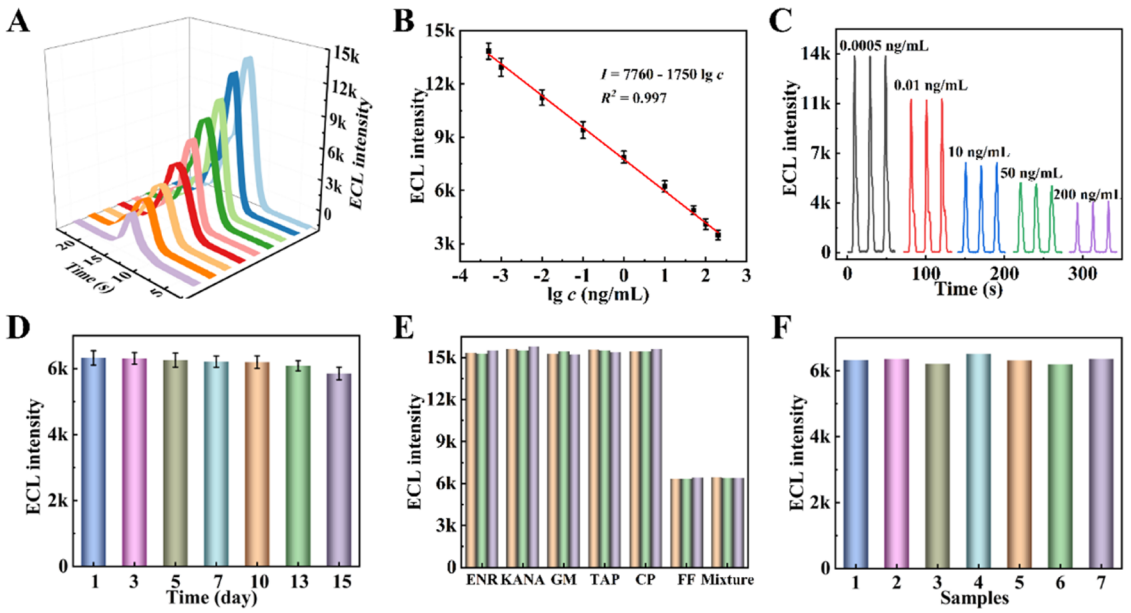


**Figure 7.** (A) ECL intensity of aptasensor with various FF concentrations (0.0005, 0.001, 0.01, 0.1, 1, 10, 50, 100, 200 ng/mL); (B) linear correlation between the logarithm of FF concentration and ECL intensity; (C) stability of aptasensor with various FF concentrations; (D) stability of aptasensor over a 15-days period with 10 ng/mL of FF; (E) specificity and (F) reproducibility of aptasensor with 10 ng/mL FF.

signal of the $ZrCuO_3$/TPrA system. Initially, $Dy_2ZnO_4$ lost electrons and underwent oxidation to form $Dy_2ZnO_4^+$ (eq 14), followed by reacting with TPrA to promote its oxidation (eq 15).

$$Dy_2ZnO_4 \rightarrow Dy_2ZnO_4^+ + e^- \quad (14)$$

$$Dy_2ZnO_4^+ + TPrA \rightarrow Dy_2ZnO_4 + TPrA^{\bullet+}(more) \quad (15)$$

**Multimodal ECL Efficiency of $ZrCuO_3$.** The multimodal relative ECL efficiency of $ZrCuO_3$ was determined with the annihilation ECL efficiency of $[Ru(bpy)_3]^{2+}$ as the reference, following the calculation outlined in the equation below

$$\Phi_{ECL} = \Phi_{ECL}^{Ru}(IQ_f^{Ru}/Q_f I^{Ru})$$

The annihilation ECL efficiency of $[Ru(bpy)_3]^{2+}$, denoted as $\Phi_{ECL}{}^{Ru}$, was set as 100%. $[Ru(bpy)_3]^{2+}$ was dissolved in an electrolyte solution of $TBAPF_6$/acetonitrile for cyclic voltammetry (CV) and annihilation ECL measurements. And the Faradaic charge $Q_f^{Ru}$ and ECL value $I^{Ru}$ of $[Ru(bpy)_3]^{2+}$ were obtained. Subsequently, $ZrCuO_3$ was tested for multimodal ECL and CV testing under different experimental parameters and electrolyte solutions (following the conditions stated in the Multimodal ECL Emission of ZrCuO3section). Multiple groups of Faradaic charge $Q_f$ and ECL signal values $I$ were obtained. The calculation based on the equation yielded the annihilation ECL efficiency of $ZrCuO_3$ as 0.5% and the cathodic ECL efficiency of $ZrCuO_3/K_2S_2O_8$ as 19.7%. Furthermore, the anodic ECL efficiency of $ZrO_2$/TPrA and $ZrCuO_3$/TPrA was determined to be 20.4 and 47.2%, which demonstrated a significant enhancement in the anodic ECL efficiency of the synthesized $ZrCuO_3$ compared to $ZrO_2$. Additionally, the relative ECL efficiency of the enhanced system $ZrCuO_3/Dy_2ZnO_4$/TPrA was measured and calculated to be 86.9%, which demonstrated a substantial increase compared to the $ZrCuO_3$/TPrA anodic ECL efficiency. Hence, utilizing the anodic ECL of $ZrCuO_3$ as the main mode, an ECL aptasensor based on the ternary system of $ZrCuO_3/Dy_2ZnO_4$/TPrA was constructed for the sensitive analysis of FF.

**Characterization and Optimization of ECL Aptasensor.** The impact of different working electrodes on the ECL performance and stability of the luminophore and the aptasensor was initially examined. Anodic ECL of $ZrCuO_3$ was tested by using both GCE and ITO as working electrodes,


https://doi.org/10.1021/acs.analchem.3c03823
Anal. Chem. 2023, 95, 17362−17371

respectively. The experimental results revealed that the use of ITO as the working electrode resulted in a more stable ECL response in comparison to the GCE (Figure S6). This observation could be attributed to the larger working area and higher conductivity of ITO. Consequently, an ITO chip was designed for aptasensor fabrication.

Circular dichroism (CD) spectroscopy was employed to investigate the recognition process between the aptamer, cDNA, and the target FF. The CD spectrum of the aptamer is shown in Figure 6A, which indicated its typical B-form conformation. Upon the addition of the cDNA, the aptamer conformation changed due to the complementary base pairing between the aptamer and cDNA, leading to a shift in the peak positions in the CD spectrum (curve b). Furthermore, in the presence of the target FF, further shifts and changes in peak positions were observed in the CD spectrum (curve c). This could be attributed to the specific recognition and binding between the aptamer and FF, leading to the separation of the aptamer from cDNA and a change in the DNA conformation.

The layer-by-layer modification of the sensing chip was characterized by using electrochemical impedance spectroscopy (EIS) (Figure 6B) and CV (Figure 6C). The bare electrode exhibited high conductivity, resulting in low impedance values and high current values (curve a). With the sequential modification of $Dy_2ZnO_4$ (curve b), cDNA (curve c), BSA (curve d), and aptamer-$ZrCuO_3$ (curve e) on the ITO electrode, the impedance values gradually increased, while the current values decreased. Finally, the addition of FF caused the detachment of aptamer-$ZrCuO_3$ from the electrode surface, leading to a reduction in the impedance values and an enhancement in the current values (curve f). The results demonstrated the successful construction of the aptasensor.

The pH, concentration of TPrA, and concentrations of $ZrCuO_3$ and $Dy_2ZnO_4$ were optimized for the sensing chip. The appropriate pH was essential to maintain the optimal state of the aptamer and cDNA and to maximize the ECL response of the sensor system. It was determined that the aptasensor exhibited the best performance at a pH of 7.4 (Figure S7A). Similarly, the concentration of TPrA significantly influenced the ECL signal of the aptasensor with the optimal concentration being 5 $\mu$L/mL (Figure S7B). Furthermore, through a series of experiments, the optimal concentrations of $ZrCuO_3$ (Figure S7C) and $Dy_2ZnO_4$ (Figure S7D) were found to be 4 and 1.5 mg/mL, respectively.

**Detection Performance of ECL Aptasensor toward FF.** The ECL aptasensor was employed for FF analysis within a concentration range of 0.0005−200 ng/mL. Figure 7A depicts a gradual decrease in ECL intensity with an increase in FF concentration. Moreover, the ECL signal of the aptasensor showed a linear correlation with the logarithm of FF concentration, described by the equation $I = 7760-1750 \lg c$ ($R^2 = 0.994$) (Figure 7B). The detection limit of the aptasensor was 0.21 pg/mL. Figure 7C demonstrates the exceptional stability of the aptasensor fabricated with varying FF concentrations. Figure S8 provides further evidence for the remarkable stability of the aptasensor with an FF concentration of 10 ng/mL after 10 cycles of the scanning test. Additionally, the ECL sensing chip displayed excellent stability over a 15-days period, confirming the superior storage stability of the designed sensing chip (Figure 7D). The aptasensor demonstrated high specificity for FF detection, as evidenced by the specificity experiments involving the interfering targets of enrofloxacin (ENR), kanamycin (KANA), gentamicin (GM), thiamphenicol (TAP), and chloroamphenicol (CP) (Figure 7E). Reproducibility testing with seven identical modified electrodes demonstrated the satisfactory reproducibility of the aptasensor (Figure 7F). To further test the reproducibility of the sensing chip, multiple sets of experiments of five batches and three different laboratories were conducted. The results showed that the sensing chip had satisfactory reproducibility (Figure S9). Furthermore, a comparative analysis with previously reported methods showed the accurate and sensitive detection capabilities of the proposed approach for FF detection, as summarized in Table S1.

**Analysis of Lake Water Samples.** The antibiotic FF in lake water was analyzed by using the standard addition method. Initially, lake water samples were collected and analyzed for FF content. The results indicated the absence of FF residue in the lake water. Subsequently, FF standard solutions were added to the samples and detected by using the sensing chip. The exceptional analysis performance of the aptasensor toward FF is displayed in Table 1, with recoveries ranging from 95 to 105% and relative standard deviation (RSD) values below 5%. These results underscore the significant potential of the aptasensor for precise and reliable FF detection in lake water samples.

**Table 1. Preliminary Evaluation of FF in Lake Water**

| samples | addition (ng/mL) | detection average (ng/mL, $n$ = 9) | RSD (%) | recovery (%) |
|---|---|---|---|---|
| lake water | 0.00 | | | |
| | 0.50 | 0.52 | 4.3 | 103.0 |
| | 1.00 | 0.96 | 3.6 | 96.0 |
| | 5.00 | 5.05 | 2.5 | 101.1 |

## CONCLUSIONS

This study offered a bandgap-regulated ECL enhancement strategy to improve the ECL efficiency of the $ZrO_2$. The ECL emitter $ZrCuO_3$ with a narrower bandgap is demonstrated to effectively enhance electron transport rate and ECL performance. Furthermore, the multimodal ECL emission of $ZrCuO_3$ was thoroughly investigated, which held significant implications for the advancement of ECL analysis. Based on the anodic ECL as the primary mode, an aptasensor chip with a signal "off−on−off" was designed for sensitive analysis of FF. This work significantly enhanced the overall performance and expanded the applicability of Zr-based oxides in the development of sensor technology. In addition, the development of $ZrCuO_3$ ECL luminophore is of great significance for their future applications in clinical analysis, medical detection, and other fields.

## ASSOCIATED CONTENT

### Supporting Information

The Supporting Information is available free of charge at https://pubs.acs.org/doi/10.1021/acs.analchem.3c03823.

Reagents and materials; apparatus; measurement parameters of ECL aptasensor and electrochemical measurement parameter; and supporting figures and table (PDF)



https://doi.org/10.1021/acs.analchem.3c03823
Anal. Chem. 2023, 95, 17362−17371

## AUTHOR INFORMATION


### Corresponding Authors

**Nuo Zhang** − *Key Laboratory of Interfacial Reaction & Sensing Analysis in Universities of Shandong, Collaborative Innovation Center for Green Chemical Manufacturing and Accurate Detection, School of Chemistry and Chemical Engineering, University of Jinan, Jinan 250022, P. R. China*; Email: zhangnuoujn@163.com

**Faying Li** − *School of Chemistry and Pharmaceutical Engineering, Shandong First Medical University & Shandong Academy of Medical Sciences, Taian 271016, P. R. China*; Email: lifaying89@163.com

**Qin Wei** − *Key Laboratory of Interfacial Reaction & Sensing Analysis in Universities of Shandong, Collaborative Innovation Center for Green Chemical Manufacturing and Accurate Detection, School of Chemistry and Chemical Engineering, University of Jinan, Jinan 250022, P. R. China; Department of Chemistry, Sungkyunkwan University, Suwon 16419, Republic of Korea*; orcid.org/0000-0002-3034-8046; Email: sdjndxwq@163.com

### Authors

**Xue Dong** − *Key Laboratory of Interfacial Reaction & Sensing Analysis in Universities of Shandong, Collaborative Innovation Center for Green Chemical Manufacturing and Accurate Detection, School of Chemistry and Chemical Engineering, University of Jinan, Jinan 250022, P. R. China*

**Xiaoyue Zhang** − *Key Laboratory of Interfacial Reaction & Sensing Analysis in Universities of Shandong, Collaborative Innovation Center for Green Chemical Manufacturing and Accurate Detection, School of Chemistry and Chemical Engineering, University of Jinan, Jinan 250022, P. R. China*

**Xiang Ren** − *Key Laboratory of Interfacial Reaction & Sensing Analysis in Universities of Shandong, Collaborative Innovation Center for Green Chemical Manufacturing and Accurate Detection, School of Chemistry and Chemical Engineering, University of Jinan, Jinan 250022, P. R. China*; orcid.org/0000-0002-4321-4282

**Hongmin Ma** − *Key Laboratory of Interfacial Reaction & Sensing Analysis in Universities of Shandong, Collaborative Innovation Center for Green Chemical Manufacturing and Accurate Detection, School of Chemistry and Chemical Engineering, University of Jinan, Jinan 250022, P. R. China*; orcid.org/0000-0002-7061-8944

**Huangxian Ju** − *Key Laboratory of Interfacial Reaction & Sensing Analysis in Universities of Shandong, Collaborative Innovation Center for Green Chemical Manufacturing and Accurate Detection, School of Chemistry and Chemical Engineering, University of Jinan, Jinan 250022, P. R. China; State Key Laboratory of Analytical Chemistry for Life Science, School of Chemistry and Chemical Engineering, Nanjing University, Nanjing 210023, P. R. China*; orcid.org/0000-0002-6741-5302

Complete contact information is available at: https://pubs.acs.org/10.1021/acs.analchem.3c03823


### Notes

The authors declare no competing financial interest.

## ACKNOWLEDGMENTS

This study was supported by the National Natural Science Foundation of China (nos. 22206056 and 22274062), the Shandong Provincial Natural Science Foundation (nos. ZR2022QB117 and ZR2022MB089), and the Jinan Scientific Research Leader Workshop Project (no. 2019GXRC027). The authors thank Shiyanjia Lab (www.shiyanjia.com) for XPS analysis.

## REFERENCES


(1) Junior, G. B.; de Souza, C. F.; da Silva, H. N.; Bianchini, A. E.; Rodrigues, P.; da Costa, S. T.; Heinzmann, B. M.; Cargnelutti, J. F.; Baldisserotto, B. *Aquaculture* **2021**, *545*, No. 737247, DOI: 10.1016/j.aquaculture.2021.737247.

(2) Shi, F.; Huang, Y.; Yang, M.; Lu, Z.; Li, Y.; Zhan, F.; Lin, L.; Qin, Z. *Front. Immunol.* **2022**, *13*, No. 970125, DOI: 10.3389/fimmu.2022.970125.

(3) Wang, J.; Wang, X.; Zheng, X.; Yang, Y.; He, Z.; Zhang, L.; Liao, Q. *Sci. Total Environ.* **2022**, *847*, No. 157444.

(4) Zeng, Q.; Liao, C.; Terhune, J.; Wang, L. *Microbiome* **2019**, *7* (1), 155.

(5) Mallik, S. K.; Shahi, N.; Pathak, R.; Kala, K.; Patil, P. K.; Singh, B.; Ravindran, R.; Krishna, N.; Pandey, P. K. *Front. Pharmacol.* **2023**, *14*, No. 1033170.

(6) Yang, M.; Li, S.; Wang, M.; Zhou, J.; Liu, Q.; Zhang, L.; Wang, T. *Microchem. J.* **2021**, *168*, No. 106330.

(7) Yuan, X.; Liu, J.; Li, R.; Zhou, J.; Wei, J.; Jiao, S.; Wang, Z. A.; Du, Y. *Molecules* **2020**, *25* (24), 6043.

(8) Yin, B.; Tan, S.; Wang, J.; Pan, K.; Wang, W.-X.; Wang, X. *Sci. Total Environ.* **2022**, *819*, No. 152946.

(9) Xia, M.; Wang, J.; Li, S.; Lin, A.; Yao, Q.; Guo, Z.; Chen, X.; Chen, Q.; Chen, X. *Sens. Actuators, B* **2023**, *393*, No. 134192, DOI: 10.1016/j.snb.2023.134192.

(10) Xia, M.; Yang, X.; Jiao, T.; Oyama, M.; Chen, Q.; Chen, X. *Food Chem.* **2022**, *381*, No. 132276.

(11) Wang, J.; Xia, M.; Wei, J.; Jiao, T.; Chen, Q.; Chen, Q.; Chen, X. *Sens. Actuators, B* **2023**, *382*, No. 133532, DOI: 10.1016/j.snb.2023.133532.

(12) Wang, J.; Li, S.; Wei, J.; Jiao, T.; Chen, Q.; Oyama, M.; Chen, Q.; Chen, X. *J. Agric. Food. Chem.* **2023**, *71* (31), 12052−12060.

(13) Cui, H.; Zhong, L.; Lv, Y.; Hao, F.; Liu, P.; Xiong, W.; Xiong, S.; Liu, H.; Luo, Ha. *Fuel* **2022**, *317*, No. 123551.

(14) Aziz, F. F. A.; Jalil, A. A.; Hassan, N. S.; Hitam, C. N. C.; Rahman, A. F. A.; Fauzi, A. A. *J. Hazard. Mater.* **2021**, *401*, No. 123277.

(15) Su, Y. H.; Jing, P. P.; Li, Y. X.; Ma, D. L.; Yue, F. Y.; Leng, Y. X. *Ceram. Int.* **2023**, *49* (3), 4109−4118.

(16) Liu, K.; Wang, G.; Guo, S.; Liu, J.; Qu, W.; Liu, N.; Wang, H.; Ji, J.; Chu, P. K.; Gu, B.; Zhang, W. *Colloids Surf., B* **2020**, *193*, No. 111074, DOI: 10.1016/j.colsurfb.2020.111074.

(17) Das, R. S.; Kumar, A.; Wankhade, A. V.; Peshwe, D. R. *Carbohydr. Polym.* **2022**, *278*, No. 118940.

(18) Wang, Q.; Edalati, K.; Koganemaru, Y.; Nakamura, S.; Watanabe, M.; Ishihara, T.; Horita, Z. *J. Mater. Chem. A* **2020**, *8* (7), 3643−3650.

(19) Dong, X.; Zhao, G.; Li, Y.; Zeng, Q.; Ma, H.; Wu, D.; Ren, X.; Wei, Q.; Ju, H. *Anal. Chem.* **2022**, *94* (37), 12742−12749.

(20) Dong, X.; Zhang, X.; Du, Y.; Liu, J.; Zeng, Q.; Cao, W.; Wei, Q.; Ju, H. *Biosens. Bioelectron.* **2023**, *236*, No. 115437.

(21) Dai, Y.-X.; Li, Y.-X.; Zhang, X.-J.; Cosnier, S.; Shan, D. *ACS Appl. Mater. Interfaces* **2023**, *15* (4), 6228−6233.

(22) Wang, M.; Liu, J.; Liang, X.; Gao, R.; Zhou, Y.; Nie, X.; Shao, Y.; Guan, Y.; Fu, L.; Zhang, J.; Shao, Y. *Anal. Chem.* **2021**, *93* (10), 4528−4535.

(23) Zhao, L.; Wang, M.; Song, X.; Liu, X.; Ju, H.; Ai, H.; Wei, Q.; Wu, D. *Chem. Eng. J.* **2022**, *434*, No. 134691.

(24) Yuan, R.; Liu, Q.; Hong, H.; Ma, H.; Xiao, L.; Li, Y.; Jiang, D.; Hao, N.; Wang, K. *J. Hazard. Mater.* **2022**, *434*, No. 128877.

(25) Li, L.; Zhao, W.; Wang, Y.; Liu, X.; Jiang, P.; Luo, L.; Bi, X.; Meng, X.; Niu, Q.; Wu, X.; You, T. *J. Hazard. Mater.* **2023**, *457*, No. 131558.

(26) Xia, H.; Zheng, X.; Li, J.; Wang, L.; Xue, Y.; Peng, C.; Han, Y.; Wang, Y.; Guo, S.; Wang, J.; Wang, E. *J. Am. Chem. Soc.* **2022**, *144* (17), 7741−7749.
(27) Zhang, P.; Shen, Q.; Wang, J.; Yu, M.; Kang, Q.; Zhang, W.; Zou, G. *Anal. Chem.* **2023**, *95* (26), 10096−10104.
(28) Chen, S.; Ma, H.; Padelford, J. W.; Qinchen, W.; Yu, W.; Wang, S.; Zhu, M.; Wang, G. *J. Am. Chem. Soc.* **2019**, *141* (24), 9603−9609.
(29) Wong, J. M.; Zhang, R.; Xie, P.; Yang, L.; Zhang, M.; Zhou, R.; Wang, R.; Shen, Y.; Yang, B.; Wang, H.-B.; Ding, Z. *Angew. Chem., Int. Ed.* **2020**, *59* (40), 17461−17466.
(30) Ouyang, X.; Wu, Y.; Guo, L.; Li, L.; Zhou, M.; Li, X.; Liu, T.; Ding, Y.; Bu, H.; Xie, G.; Shen, J.; Fan, C.; Wang, L. *Angew. Chem., Int. Ed.* **2023**, *62* (21), No. e202300893.
(31) Xu, W.; Wu, Y.; Wang, X.; Qin, Y.; Wang, H.; Luo, Z.; Wen, J.; Hu, L.; Gu, W.; Zhu, C. *Angew. Chem., Int. Ed.* **2023**, *62* (29), No. e202304625, DOI: 10.1002/anie.202304625.
(32) Ji, K.; Wang, Y.; Mao, L.; Wang, Y.; Zhang, X. *Sens. Actuators, B* **2021**, *345*, No. 130405, DOI: 10.1016/j.snb.2021.130405.
(33) Yang, F.; Yang, F.; Tu, T.-T.; Liao, N.; Chai, Y.-Q.; Yuan, R.; Zhuo, Y. *Biosens. Bioelectron.* **2021**, *173*, No. 112820.
(34) Wang, H.; Zhang, R.; Zhuo, Y.; Yuan, R. *Anal. Chim. Acta* **2021**, *1188*, No. 339181.
(35) Cai, L.; Wang, H.; Cao, Y.; Hao, W.; Fang, G.; Wang, S. *Biosens. Bioelectron.* **2023**, *234*, No. 115336.
(36) Liu, Q.; Song, Y.; Ma, Y.; Zhou, Y.; Cong, H.; Wang, C.; Wu, J.; Hu, G.; O'Keeffe, M.; Deng, H. *J. Am. Chem. Soc.* **2019**, *141* (1), 488−496.
(37) Li, Y.-F.; Wang, D.; Liao, Z.; Kang, Y.; Ding, W.-H.; Zheng, X.-J.; Jin, L.-P. *J. Mater. Chem. C* **2016**, *4* (19), 4211−4217.
(38) Hu, Q.; Cheng, X.; Zhang, X.; Xu, Y.; Gao, S.; Zhao, H.; Major, Z.; Huo, L. *Sens. Actuators, B* **2020**, *305*, No. 127434, DOI: 10.1016/j.snb.2019.127434.
(39) Abu-Zied, B. M.; Asiri, A. M. *J. Rare Earths* **2014**, *32* (3), 259−264.
(40) Rizzo, F.; Polo, F.; Bottaro, G.; Fantacci, S.; Antonello, S.; Armelao, L.; Quici, S.; Maran, F. *J. Am. Chem. Soc.* **2017**, *139* (5), 2060−2069.
(41) Wang, C.; Li, Z.; Ju, H. *Anal. Chem.* **2021**, *93* (44), 14878−14884.
(42) Dong, X.; Zeng, Q.; Dai, L.; Ren, X.; Cao, W.; Ju, H.; Wei, Q. *Anal. Chem.* **2023**, *95* (32), 12184−12191.


https://doi.org/10.1021/acs.analchem.3c03823
*Anal. Chem.* 2023, 95, 17362−17371